Nearsightedness of Crystalline Materials and Intergranular Embrittlement

M. Rajivmoorthy[a], **T. R. Wilson**[a], **and M. E. Eberhart**[a,*]

[a]Molecular Theory Group, Colorado School of Mines, Golden, Colorado, USA; [*]To whom correspondence should be addressed. E-mail: meberhar@mines.edu

This manuscript was compiled on January 26, 2022

Our quest to design materials often envisions as a first step the conceptual decomposition of a material into meaningful atomic scale neighborhoods. The performance of the monolithic material is then seen to arise from the combined properties of these much simpler regions. It is the nearsightedness of electronic matter (NEM) principle that provides the rigorous justification for this "divide and conquer" approach. NEM asserts that a material property may be significantly affected by a perturbation, no matter how large, only over a neighborhood of size R. Though NEM posits the existence of meaningful atomic scale neighborhoods, for the most part these regions are identified empirically. In this paper we propose a methodology to divide real materials into meaningful neighborhoods determined by the topology of the charge density. We generalize this approach by applying the same to determine neighborhoods representative of elemental crystalline materials and then use these neighborhoods to model the embrittling effects of bismuth atoms segregated to copper grain boundaries. We show that embrittlement is the result of impurity atom-induced enhancements of copper nearsightedness. We further suggest that just as nearsightedness plays an overlooked role mediating embrittlement, it may also be an important factor affecting a broad range of unresolved problems as apparently diverse as energy focussing phenomena and enzyme kinetics.

Keywords: divide and conquer | nearsightedness | molecular and materials design | grain boundary | computational chemistry

1. Introduction

The performance of structural materials derives from the way strain energy is distributed among the material's many defects and other heterogeneities. While elasticity theory and continuum mechanics are useful in describing the effects of defects on the long-range distribution of strain, the effects due to atomic scale fluctuations are poorly understood. As a quintessential example, normally ductile materials like copper and iron become brittle in the presence of even minuscule quantities of elements such as hydrogen or sulfur. Obviously, embrittling elements alter the distribution of strain energy, though the question of how these effects are produced remains open.

Embrittlement is but one technologically important problem in the broader class of phenomena controlled by atomic scale influences to the energy of an applied perturbation. While developing a more fundamental understanding of the mechanisms responsible for these processes would enhance our ability to select compositions to optimized materials properties, the diversity of defects and heterogeneities that must be considered makes this a daunting task. Even so, investigators are pursuing methodologies intended to systematize this effort. One such approach appeals to the nearsightedness of electronic matter principle (NEM), which asserts that the properties of complex materials can be considered to arise piecewise from local neighborhoods.[1–3] In this approach, neighborhoods may be investigated one at a time using "divide and conquer" techniques through which large and complex molecules and solids are decomposed (divided) into neighborhoods with comprehensible properties (conquered).[4]

NEM derives its name from the observation that atoms "see clearly" only nearby atoms. Rigorously, it posits that for a fixed chemical potential the charge density, $\rho(\boldsymbol{r})$, and local properties originating from $\rho(\boldsymbol{r})$ are sensitive to changes to the external potential within some radius R. Changes to the potential beyond R—no matter how large—do not significantly affect the density.[2] In other words, there is a monotonically decreasing function, $\Delta\rho(\Omega_{\boldsymbol{r}_0}, R)$, giving the cumulative density change over a connected region Ω about $\boldsymbol{r}_0$ due to a perturbation of any magnitude at R, such that $\lim_{R\to\infty} \Delta\rho = 0$. As a useful corollary, if Ω is a region over

which the energy is well-defined, then there is a function $\Delta\varepsilon_\Omega(R)$ giving the energy change of Ω due to a perturbation of any magnitude a distance R from Ω such that $\lim_{R\to\infty}\Delta\varepsilon_\Omega = 0$.

In its energy form NEM provides the means to locate atomic neighborhoods from which a property, p, originates. One begins by isolating a region Ω of radius R_Ω from its larger molecule or solid. In principle one may calculate the energy of this isolated region and the change to its energy as the atomic environment at successively greater distances from Ω are restored. At some R, designated R_p, $\Delta\varepsilon_\Omega$ becomes small relative to the property's characteristic energy. In this way, the property may be argued to emerge from the atomic structure of a neighborhood of radius $R_\Omega + R_p$, where R_p is ostensibly the width of the boundary separating Ω from a free surface.

Equally consequential, the electronic structure of these local neighborhoods may be considered essentially independent, making it possible to use massively parallel algorithms to calculate the structure of large and complex materials.[1,5–7] The inherent inaccuracy associated with such schemes depends on the magnitude of $\Delta\varepsilon_\Omega(R_p)$, which NEM asserts decreases as R_p increases. For such calculatons the size of neighborhoods and the widths of their boundaries are chosen so as to minimize computational time while achieving some desired energy accuracy. In these instances, R_p is treated as an adjustable parameter rather than a property in and of itself.

Here we report our efforts to directly calculate $\Delta\varepsilon_\Omega(R)$ across a series of crystalline materials. We then apply these findings to identify the atomic neighborhoods mediating metallic grain boundary properties and, using the copper bismuth system as an example, show that nearsightedness plays an important role mediating the effects of impurities to a material's mechanical properties.

2. Calculations and Results

Approximately eighty clusters representing crystals of eleven elements were constructed from a central atom and its first n coordination shells (concentric spheres containing the nearest neighbor atoms, the second nearest neighbor atoms, and so on to the n^{th} nearest neighbors) with n varying from 0 to as large as 11. We defined the region Ω, also called the central cluster, to be a central atom and its first coordination shell.

These clusters were then modeled with DFT methods provided within the SCM chemistry and materials modeling suite (see SI for more details).[8–11] The per atom energy of Ω was found using Bader partitioning.[12,13] Through this combination of techniques we were able to calculate an effective central atom energy as perturbed by an increasing number of coordination spheres designated E_n^x, where x indicates the element and n the number of coordinations spheres surrounding the central atom. The perturbation energy to this effective central atom as a function of n is then given by $E_n^x - E_0^x \equiv \Delta E_n^x$. A zero of energy may be established by noting that as n grows without bound, ΔE_n^x will approach the crystal's formation energy, E_f^x, a quantity readily computed using band methods. Consequently, we define a nearsightedness function $\Delta\varepsilon_n^x \equiv \mid E_f^x - \Delta E_n^x \mid$ and note that $\lim_{n\to\infty}\Delta\varepsilon_n^x = 0$. A property dependent nearsightedness distance can be extracted from this funtion as the values of n for which $\Delta\varepsilon_n^x$ becomes smaller than the characteristic energy of the property of interest.

We constructed our computations in three sets of increasing computational complexity and hence accompanied by greater imprecision in the calculated form of the nearsightedness function. Using these constructions, we were able to apply what was learned from the less complex models to deduce trends to the form of $\Delta\varepsilon_n^x$ that may have eluded us had we

proceeded directly to the final calculations. The first set of calculations determined $\Delta\varepsilon_n^x$ of four comparatively light crystals: diamond cubic (DC) silicon, a prototype covalent material; face centered cubic (FCC) aluminum, a free electron metal; FCC copper, a d-block metal with a full d-band; and body centered cubic (BCC) vanadium, a metal with a partially occupied d-band. The elements of the second set were drawn from the heavier $4d$ transition metals and contain the BCC metals niobium and molybdenum; the hexagonal close packed (HCP) metals technetium and ruthenium; and the FCC metals rhodium, palladium, and silver. Compared to set 1, larger basis sets, necessary to model these crystals, were unavailable, introducing basis set error in the determination of the crystalline formation energy. And for the third set we modeled a pure copper grain boundary along with the same boundary containing bismuth atoms. The complicating factor for this set of calculations was to assess the effect of non-crystallinity on the nearsightedness function.

Table 1. The diamond cubic (DC) shell structure. Row 1: Number of the coordination shell. Coordination shell zero is the central atom. Row 2: Number of atoms in coordination shell n. Row 3: Total number of atoms in the cluster of n coordination shells. (Hard sphere representations of some of these clusters are provided in the SI.) Row 4: Radius of the cluster, i.e. distance between the central atom and the atoms of the n^{th} shell in atomic diameters or equivalently nearest neighbor separations.

Coordination shell n	**0**	**1**	**2**	**3**	**4**	**5**	**6**	**7**	**8**	**9**	**10**	**11**
Number of n^{th} neighbors	0	4	12	12	6	12	24	16	12	24	12	8
Total atoms in cluster	1	5	17	29	35	47	71	87	99	123	135	143
Cluster radius	0	1	$2\sqrt{\frac{2}{3}}$	$\sqrt{\frac{11}{3}}$	$4\sqrt{\frac{1}{3}}$	$\sqrt{\frac{19}{3}}$	$2\sqrt{2}$	3	$4\sqrt{\frac{2}{3}}$	$\sqrt{\frac{35}{3}}$	$\sqrt{\frac{43}{3}}$	4

Table 2. Si atomic diameter, energy of formation, isolated atomic energy, and changes in central Bader atom energy resulting from the addition of cluster coordination spheres (ΔE_n^x) as described in the text. Distances are reported in Å and energies in eV. ΔE_{10} was not determined.

Si diameter (Å)	E_f	E_0	ΔE_1	ΔE_2	ΔE_3	ΔE_4	ΔE_5	ΔE_6	ΔE_7	ΔE_8	ΔE_9	ΔE_{11}
2.352	-5.42	-7865.72	-3.05	-9.01	-5.66	-5.55	-6.09	-6.71	-6.67	-6.12	-5.91	-5.79

A. Silicon, Aluminum, Vanadium and Copper. Silicon possesses the diamond cubic crystallographic structure. Its near neighbor shell structure is summarized in Table 1, with the central crystalline region represented by a five atom cluster (Si_5) composed of a single atom and its four tetrahedrally coordinated nearest neighbors.

Relative to the energy of an isolated Si atom, E_0, the calculated per atom Bader energy of Si_5 as its boundary region was increased to include a second, third, fourth and so on up to eleven coordination shells are reported in Table 2 along with the nearest neighbor distance of Si and its calculated formation energy, E_f.

These results are summarized graphically in the upper left of Fig. 1 where $\Delta\varepsilon^{\text{Si}}$ is depicted as a function of n. This figure represents the sensitivity of the central cluster to the retreating perturbation, that is, the distance over which the central cluster can clearly see the free surface. When the energy goes to zero, from the central cluster's point of view, the surface has vanished. Plainly, when the free surface is infinitely distant from the central cluster, the cluster's per atom energy will be identical to that of crystalline Si. Hence beyond some point, to computational accuracy, the decay of $\Delta\varepsilon$ will approach zero asymptotically. In fact, because for both ordered and disordered gapped materials—the systems modeled here are all gapped, in that the central cluster energy converges to within computational accuracy before the energy difference between the LUMO and HOMO is on the order of kT—the change in the density due to a perturbation at R decays exponentially with R,[2] it is arguable that energy

decay should not only be asymptotic but exponential.

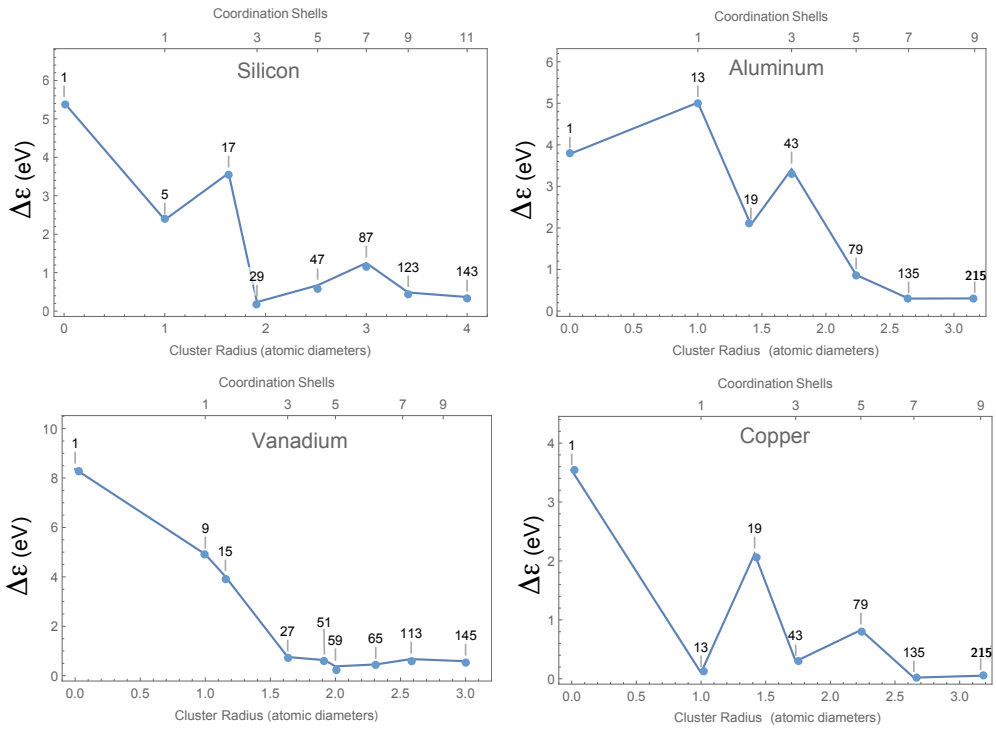

Fig. 1. The nearsightedness function ($\Delta\varepsilon_n^x$) for the elements Al, Si, V and Cu as a function of n. The callouts in the graphs give the number of atoms in the representative cluster. For example, an Al cluster representing a central atom and its first 7 coordination spheres will contain 135 atoms.

Regardless, inspection of Fig. 1 reveals that the onset of the asymptotic/exponential decay begins with coordination shell seven, where the per atom energy difference between crystalline silicon and the central cluster is on the order of an eV, decreasing to 0.36 eV at eleven coordination shells—three atomic diameters beyond the central cluster.

Naturally, this variation of $\Delta\varepsilon$ is due to the changing boundary width and its associated influence on the central cluster charge density.[14] And just as the energy of a central cluster with an infinite boundary will be equivalent to that of a crystal, so too will the charge density of a cluster with an infinitely wide boundary be identical to the crystalline density.

For all elemental crystals, equivalence between the central cluster and crystalline charge densities is required when the Bader atom surfaces of the central cluster are coincident with the crystalline Voronoi polyhedra (cells) about each atom. Quite generally, the difference between the surface of a cluster's Bader atoms and a crystal's Voronoi cells provides a measure of their charge density differences, which vanish when the two surfaces coincide.[15]

A Bader atom's surface must contain local charge density minima. (In the chemical literature[12] these minima are called cage critical points to indicate that there is one such point interior to cages of bound atoms.) Plainly, an atom's local charge density minima may be a finite or an infinite distance from the atomic nucleus. If all the local minima are a finite distance from the nucleus, the surface of the Bader atom is topologically connected and the atom is said to be closed. On the other hand, if even one local minimum is located at infinity, the Bader atom surface is disconnected and the atom is said to be open. Importantly, for any open Bader atom there is a path lying entirely within the atom that runs from the location of the nucleus to a point at infinity. Quite simply, an open atom is characterized by a channel of

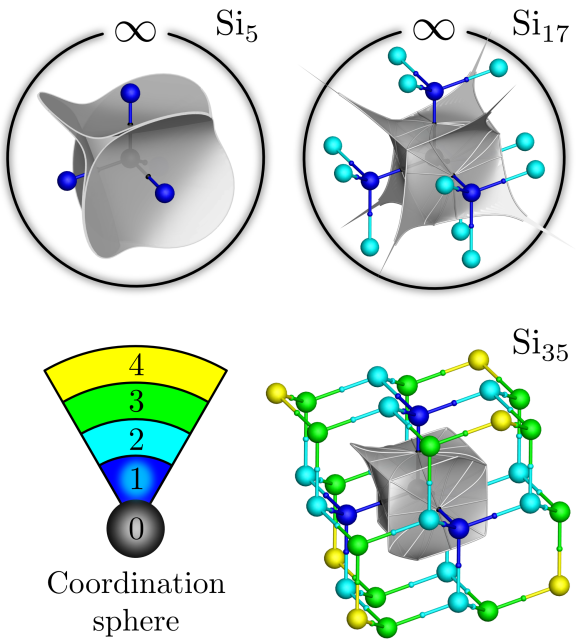

Fig. 2. Depiction of the central Bader atom surfaces in 5, 17, and 35 atom clusters (1, 2, and 4 coordination spheres respectively). Nuclear positions are indicated by spheres colored according to coordination sphere. In Si_5 (top-left) the central Bader atom remains clearly open in four regions, one of which is facing to the left of center, while elsewhere the Bader atom surfaces are essentially converged. With two coordination spheres (top-right; Si_{17}) those same open regions have closed coincident with topological cage points, and only slivers of very-nearly converged surfaces prevent the Bader atom from being closed. At four coordination spheres (bottom-right; Si_{35}) the Bader atom has closed completely. The open surfaces in Si_5 were truncated according to the $0.001e^-$ charge density isosurface.

charge density connecting the nucleus to the neighborhood of at least one infinitely distant point. In contrast, the surfaces of crystalline Voronoi polyhedra are necessarily connected. For example, the Voronoi cell of the diamond cubic structure is in a class of truncated tetrahedra.

As a means of clarifying this issue, consider the evolution of a central region's Bader atoms as a cluster grows.[14] In the case of Si, this process is represented in Fig. 2. The top-left frame depicts the Bader atom surfaces of Si_5, or equivalently the interatomic boundaries between the central atom and its first coordination sphere. This set of surfaces is constructed from four asymptotic—hence disconnected—surfaces. As a result, all the Bader atoms of the Si_5 cluster are open. In other words, around every point there is a direction in which the charge density is decreasing and thus local minima are infinitely distant from the central atom.

The boundary of the central Bader atom evolves with the addition of the twelve atom second coordination sphere to yield the Si_{17} cluster pictured in the top-right frame of Fig. 2. While the asymptotes separating the surfaces of this atom become steeper, the central Bader atom still extends to infinity. In other words, from some points near the central atom there is a path of decreasing charge density that leads to infinity. This path will be located within the "spikes" evident in the top-right frame of Fig. 2.

As depicted in the bottom-right frame of Fig. 2, it is with the addition of the fourth coordination sphere to make a Si_{35} cluster that the boundary of the central Bader atom is topologically connected and the atom is closed. It is at this point that the cages of bound atoms sharing the central atom as a common vertex are completed, which mandates a single local minimum at the center of each of these cages. In a sense, it is with the completion of these cages, and the resultant closing of its Bader atom, that the central atom becomes isolated from the surroundings through an intervening shell of charge density.

While the central atom is closed with the fourth coordination shell, the central cluster closes at the seventh coordination shell, *i.e.* Si_{87}. It is here that the cages having a first coordination

sphere atom as a vertex are completed. In fact, at this point the Bader atoms of the central cluster possess the topology of the Voronoi polyhedra of crystalline silicon. And, though Fig. 1 shows only a few points beyond the seventh coordination shell, $\Delta\varepsilon$ decreases monotonically (arguably exponential decay) through these points.

Returning to the remaining crystals of the first set: Al, V, and Cu. The central cluster of the FCC metals (Al and Cu) is a cuboctahderon consisting of a central atom and its twelve nearest neighbors. The central cluster of BCC V is a nine atom cube with an atom at the cube center and its eight nearest neighbors located at the cube vertices. Pictures of these clusters along with analogues of Table 1 giving more information regarding the shell structure of FCC and BCC crystals along with the element specific cluster energy analogues of Table 2 are provided in the SI.

This information is also summarized graphically in Fig. 1 where $\Delta\varepsilon_n$ for the central cluster of each element is plotted as a function of n. In all cases, within ten coordination spheres $\Delta\varepsilon$ converged to within a fraction of an eV of the computed crystalline formation energy ($\Delta\varepsilon_9^{\mathrm{Al}},\ \Delta\varepsilon_{10}^{\mathrm{V}},\ \Delta\varepsilon_9^{\mathrm{Cu}} = 0.30,\ 0.58,\ 0.05$ eV respectively). More noteworthy however, though the onset of exponential decay is element dependent—2, 3, and 5 coordination spheres for V, Al, and Cu respectively—beyond the point where the Bader atoms of the central cluster close (BCC clusters of 59 atoms and FCC clusters of 79 atoms) $\Delta\varepsilon$ is monotonically decreasing or level.

B. 4*d* Metals. The heavier $4d$ transition metals required a larger basis set for the accurate determination of Bader atom energies. Unfortunately, the use of this larger basis set introduced an estimated 0.6 eV imperscision (see SI) to the calculated values of the crystalline formation energy. Nonetheless, ΔE as a function of the number of coordination shells for the BCC metals Nb and Mo; the FCC metals Rh, Pd and Ag; and the HCP metals Tc and Rh are shown in Fig. 3. The information contained in these figures is provided in tabular form in the SI.

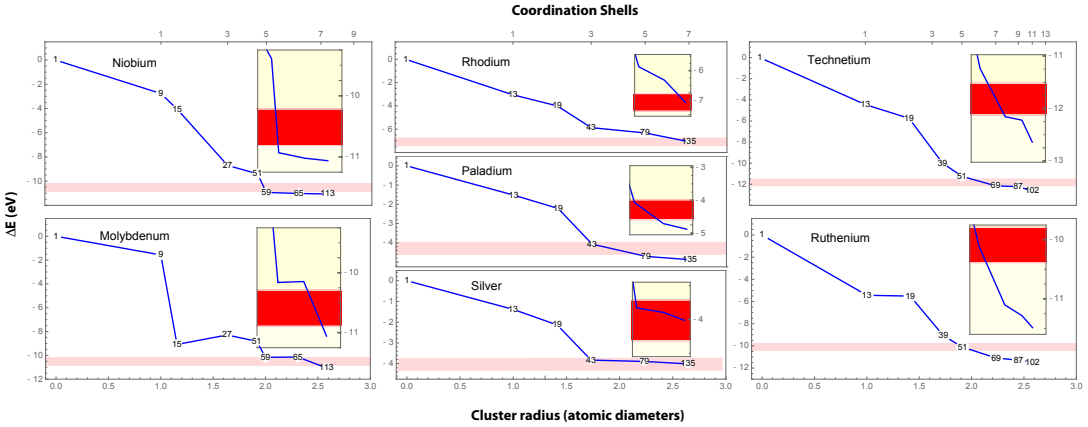

Fig. 3. The change in central Bader atom energy resulting from additional cluster coordination shells (ΔE) for the BCC (left column), FCC (center column) and HCP (right column) $4d$ transition metals. The red stripes indicate the crystalline formation energy assuming a ± 0.3 eV basis set error. Insets provide a higher fidelity depiction of ΔE for the three largest clusters of the series.

Like the first set of crystals, all metals appear to be converging asymptotically on a value near their estimated formation energies for clusters with radii of 2.5 atomic diameters. More significant however, across a given structure type–BCC, FCC, HCP—the form of the decay of ΔE is similar. This is particularly noticeable for the BCC metals Nb and Mo.

Recall the central nine atom cluster of a BCC metal closes at 59 atoms or equivalently five coordination spheres. Figure 3 reveals a rapid decrease of more than an eV in the central cluster energy on addition of the fifth coordination sphere—transforming a 51 to a 59 atom cluster; and for both Nb and Mo bringing the central cluster energy to within computational accuracy of the estimated formation energy. While in V the effect is not as dramatic, a similar central cluster stabilization was observed (Fig. 1) with the addition of the fifth coordination sphere.

The decay of $\Delta\varepsilon$ for the FCC metals as shown in the center column of Fig. 3 also exhibit similar forms. The most pronounced energy change accompanies the closing of the central Bader atom with the addition of the second coordination sphere, which also marks the onset of exponential decay. The closing of the central cluster at five coordination spheres and 79 atoms is well inside the "asymptotic" region of the decay and is not as sharply defined as in the $4d$ BCC metals.

Unlike the BCC metals, characterized by a single type of local minimum, the FCC metals have two; the first at the center of the FCC octahedral hole, and the second at the center of the FCC tetrahedral hole. Some of the channels linked to these minima are plugged earlier than are others. The tetrahedral holes of the central atom form with the addition of the first coordination sphere and the central atom octahedral holes with the second coordination sphere. The addition of the third coordination sphere at a cluster size of 43 atoms, which correlates with a substantial central cluster stabilization, begins closing the atoms in the first coordination sphere. Nonetheless, the central cluster fully closes only with the addition of the fifth coordination shell. And it is at this size that the energy of the central cluster falls to within 0.15 eV of the estimated formation energy for all the $4d$ FCC transition metals.

There are 4 symmetry unique local minima types in HCP clusters. Like the FCC structure there are both tetrahedral and octahedral minima. And like the FCC metals, the onset of exponential decay begins with the addition of the second coordination sphere. However, with the central cluster possessing D_{3h} symmetry, the octahedral and tetrahedral holes are split into symmetry unique pairs depending on their displacement perpendicular or parallel to the 3-fold axis. The central thirteen atom cluster undergoes significant closure with the third coordination shell and completely closes with the fifth coordination shell—a cluster of 51 atoms.

Thus, across all structure types modeled, the energy of the central cluster "improves" in lock step with the progressive closing of the central cluster. The underlying factors driving this observation are rooted in the virial theorem.[16,17]

When extended to Bader atoms[12] the virial theorem establishes that for an atom Ω at mechanical equilibrium, its average kinetic energy $\langle T_\Omega \rangle$, and its average potential energy $\langle V_\Omega \rangle$ are related by,

$$\langle V_\Omega \rangle = -2\langle T_\Omega \rangle$$

and hence its total energy E_Ω is simply,

$$E_\Omega = -\langle T_\Omega \rangle.$$

Ergo, as an atom lowers its total energy through interactions with its surroundings, its kinetic energy must simultaneously increase. However, the virial theorem applies only to average energies, therefore the regions of increased kinetic energy need not coincide with the regions of decreased total energy.

Bader argued that the "quantum mechanically local kinetic energy" at a point $\boldsymbol{r}_0$, is related to the magnitude of $\nabla^2\rho(\boldsymbol{r})|_{\boldsymbol{r}_0}$.[18] Hence, deep, steeply curved minima contribute positively to the kinetic energy and allow electron rearrangement in other regions that will lower E_Ω. Also

we note that as charge density minima lie along interatomic nodes of the one-electron wave functions, they may coincide with anti-bonding interactions where kinetic energy is high.[19]

C. Nearsightedness and Embrittlement. We conclude that "good" models of crystalline environments will at a minimum envelop a neighborhood that extends to local charge density minima and thereby recover the topology of $\rho(\boldsymbol{r})$. It is worth considering the fundamentals driving this observation.

In the cases we have considered, charge density minima and the cages they represent result from p- and d-orbital alignments in which the crystalline environment couples σ-, π- and δ-interactions so as to minimize **global energy**. Models that exclude charge density minima effectively decouple the orbital interactions to allow **local energy** minimization and hence cannot serve as good crystalline representations. However, while decoupling in crystals is an artificial effect stemming from an inadequate model, it is a real effect around defects, possibly altering the nearsightedness function and the properties mediated by nearsightedness. One such property is impurity induced embrittlement.

Impurity induced embrittlement often begins with the segregation of dilute impurities to grain boundaries, which, through a not entirely understood mechanism, yields them susceptible to brittle failure. Because this phenomena is of great economic consequence, and is often associated with catastrophic failure leading to the loss of life,[20,21] it has been extensively studied. Particularly significant are studies seeking to correlate embrittlement with changes to electronic structure caused by segregation. These studies have resulted in three proposed mechanisms. The first, posits that impurity atoms weaken the boundary by withdrawing electron density from the cohesive metal-metal bonds.[22] The second is a thermodynamic model implicating the difference between grain boundary and surface energy as the parameter controlling embrittlement potency.[23,24] According to this model, the more an element lowers surface energy relative to grain boundary energy, the greater its embrittling potential. The third model attributes embrittlement to changes in the directionality of the grain boundary bonds. In one instance, it has been argued that embrittling elements make intergranular bonds more directional,[25] and in another less directional.[26] However, none of these consider possible synergistic effects between the sites of fracture initiation and embrittling atoms.

All fractures begins in the vicinity of a stress concentrator, conventionally thought of as an atomically sharp crack.[27,28] The importance of such cracks cannot be discounted. Ductile substances may fail in an apparently brittle fashion through the introduction of a sufficiently sharp crack. On the other hand, normally brittle materials can be rendered deformable by eliminating surface cracks.[29] Traditionally such cracks are envisioned as having an easily identifiable tip, with bonds on the crack side broken and unable to carry load. An applied stress normal to the crack will of necessity concentrate in the unbroken bonds on the other side of the tip, causing them to preferentially elongate, ultimately break and thereby growing the crack. Elasticity theory attributes the stress concentration from a classical crack to its length and the radius of its tip, neither of which has meaning in a real material where instead energy localization derives from the crack tip charge density.

Owing to its comparative simplicity, bismuth doped copper serves as one prototypical system for the investigation of intergranular embrittlement.[30–34] And consequently a wealth of data has been generated on this system through both theoretical and experimental investigations.[32,34–40] Particularly important to our efforts is the study by Duscher *et al.*,[38] which included atomic resolution Z-contrast images of the grain-boundary region of a symmetric 36.8° <001> tilt boundary known to be embrittled through Bi segregation.

The structure of this boundary is shown in Fig. 4 and is characterized by a repeating kite structure. Bi was found to substitute for the Cu atom at the center of this kite where it sits in a roughly pentagonal coordination shell of 14 atoms, also shown in Fig. 4. We take this 14

atom shell containing a central Bi or Cu atom as the central cluster of our nearsightedness investigation.

As in the crystalline studies, we determined the change to the energy of this cluster through the addition of successive coordination spheres. The calculated energies are given in the SI and the results are shown graphically in Fig. 5, where the top frame gives the raw values for the two—Cu and Bi containing—clusters. The bottom frame of the figure gives the "normalized" values of $\Delta\varepsilon_n$, where the maximum value of $\Delta\varepsilon_n$ is used as a normalizing factor. This bottom frame allows one to compare the response of pure Cu and Bi segregated systems to perturbation from successive bicrystalline shells, or conversely, how a perturbation to the central cluster containing either Cu or Bi is distributed to the surrounding bicrystal.

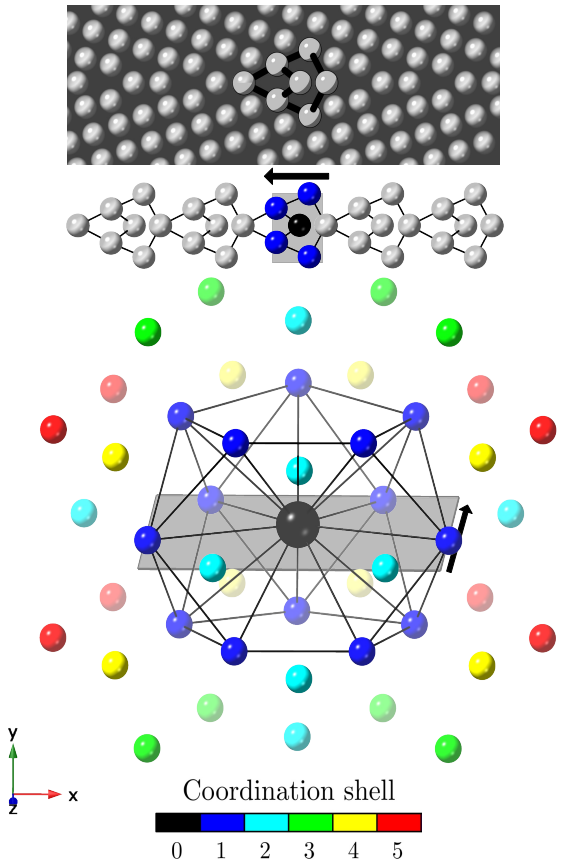

Fig. 4. Depiction of the Bi-Cu boundary cluster. A simulated image of the grain boundary region from reference 38 with the structural unit is indicated (top). The 2-dimensional repeating structural unit (middle), and the corresponding 3-dimensional cluster with the Bi atom in the center (bottom) are shown. The atoms are color coded based on coordination sphere; and the central cluster is represented by the first coordination sphere. The XZ plane, indicated by the gray plane in the bottom frame coincides with the grain boundary plane and corresponds to the grey shaded rectangle in the middle frame, where the same atom coloring is used to show the central cluster atoms in the boundary.

Unlike the crystalline systems, the central grain boundary cluster of pure Cu becomes less stable due to the perturbing influences of the surrounding environment. This behavior results from competition between interactions that lower either global or local energy. As mentioned, interactions that promote global stabilization of the FCC structure are a consequence of aligning Cu *d*-orbitals so as to maximize the combined contributions from σ-, π- and δ-overlap. Global energy minimization is highly constrained and hence the interactions responsible for this stabilization are termed directional. Local stabilization results from charge transfer between an atom and its immediate environment to bring *s*-orbitals into energy alignment and promote non-directional coulomb attraction.

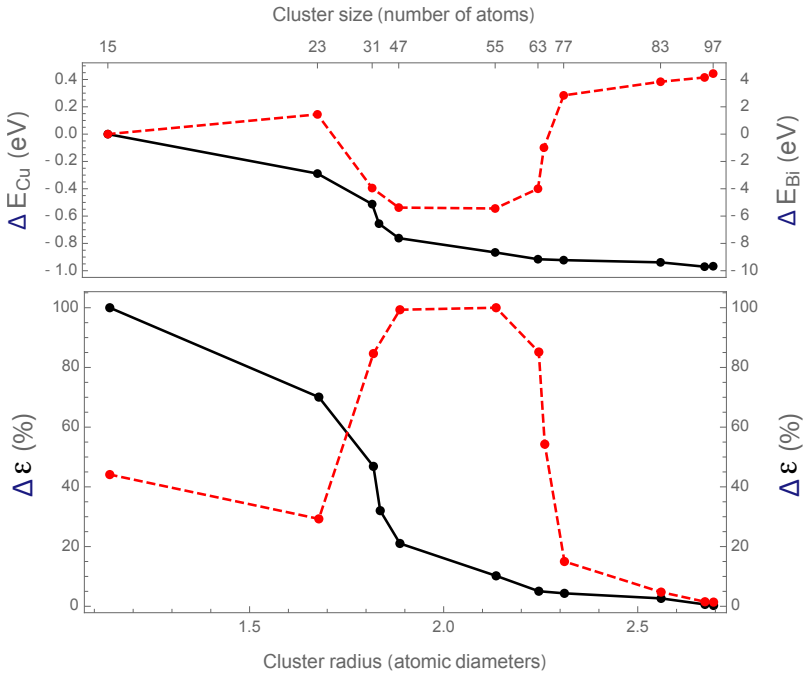

Fig. 5. Change in central cluster Bader energy resulting from additional grain boundary cluster coordination shells. **Top:** Per atom ΔE for Cu (dashed red) and Bi (solid black) centered grain boundary clusters. **Bottom:** $\Delta\varepsilon$ normalized by the respective maximum magnitudes of the perturbation energies.

For the isolated central grain boundary cluster, non-directional interactions predominate. The Cu atom at the center of the non-crystallographic 14 atom shell develops a Bader charge of 0.24 electrons that is necessarily transferred to the 14 atom shell—Hirshfield charge density analysis shows the same charge transfer. As successive shells are included in the model, the charge transfer stays essentially constant, dropping to 0.21 electrons through the 63 atom cluster, but decreasing more rapidly from that point on, reaching a value of 0.12 electrons at the 97 atom cluster.

Inspection of Fig. 5 reveals a corresponding steep change to the perturbation energy at the 63 atom cluster and a distance of roughly 2.2 Cu-Cu near neighbor separations. Remarkably, this is very near the distance at which the central cluster of crystalline Cu (see Fig. 1) fully closes with an accompanying onset of exponential energy decay. Hence beyond 2.2 Cu diameters, the perturbation to the central grain boundary cluster due to the surrounding bicrystalline environment exceeds the stability gained from the non-directional coulomb interactions. The charge density of the central cluster responds by aligning its *d*-orbitals with those of the grains on either side of the boundary, which reduces the energy of distant atoms. However, because the *d*-orbitals of the central cluster cannot be internally aligned, due to the grain boundary misorientation, the central cluster energy increases. Overall though, there is a net stabilizing effect to the system, which decays exponentially beyond 2.2 Cu diameters and becomes insignificant relative to the grain boundary energy beyond 2.5 Cu diameters. That is, movement of the atoms at the core of a pure Cu grain boundary are felt across a sphere of approximately 2.5 Cu diameters.

The Bi containing central cluster behaves similarly to the pure Cu cluster out to roughly 2.1 Cu diameters. But unlike pure Cu, the energy of the central cluster does not change substantively with increasing coordination spheres of bicrystalline environment. This response is due to the valence *p*-orbitals on the Bi atom, which combine with Cu orbitals to form

localized states that inhibit Cu atom *d*-orbitals on the central cluster from aligning with those on the adjacent grains. Effectively, the Bi containing boundary is more nearsighted than the pure Cu boundary and cannot see the bicrystalline environment beyond 2.1 (arguably 1.9) Cu diameters.

Consider now a load applied normal to an atomic scale crack that at one end intersects a Cu grain boundary. This crack will act as a stress concentrator. On the one hand, in the absence of segregated impurities, perturbations to the positions of the crack tip atoms resulting from the applied load will be distributed to a significant extent over a spherical volume with a radius of about 2.5 Cu diameters. On the other hand, in the presence of segregated Bi atoms, the same load induced perturbations will be distributed across a sphere with a radius of about 2.1 Cu diameters, a neighborhood with a volume about 60% as large as that of the impurity free boundary. For all practical purposes, Bi atoms sharpen Cu crack tips.

In the Cu-Bi system we hypothesize that embrittlement results from impurity induced nearsightedness and hence an increase to the crack tip stress intensity factor. In effect, nearsightedness is the quantum mechanical counterpart to continuum mechanics' crack tip radius. As such, increased crack tip nearsightedness, whether induced by impurities or the crack tip atomic structure itself, is also a necessary and perhaps sufficient condition for brittle fracture. Though here the mechanism responsible for enhanced nearsightedness is the result of greater non-directional bonding, resulting in local elastic constant softening—consistent with the findings of references 26 and 38—we see no reason to believe that this is the sole mechanism responsible for increased nearsightedness. More thorough investigations of nearsightedness and its underlying atomic origins may shed light not only on environmentally induced embrittling phenomena, where the composition of embrittling elements is often sharply peaked around stress concentrators, but also on intrinsic brittleness and the host of phenomena involving mechanical and chemical energy focussing and localization such as: explosive hot spot formation,[41] triboluminescence,[42] sonoluminescence,[43] sonochemistry,[44] and enzyme electrostatic preorganization.[45]

3. Summary

We have defined a nearsightedness function giving the local perturbation energy due to an increasingly distant free surface. This function allows one to identify the neighborhoods that may serve as models of crystalline and defected materials. The boundaries of these neighborhoods are determined by the topological properties of the charge density and were found to be a few atomic diameters in radius. We argued that these neighborhoods serve as adequate models for the study of many properties and particularly mechanical properties of metals. We supported this argument by demonstrating that Bi atoms segregated to a Cu grain boundary increase nearsightedness and suggested that enhanced nearsightedness manifests most prominently through increases to the crack tip stress intensity factors. We further proposed that the nearsightedness function may prove useful in investigations of diverse phenomena involving energy focussing and localization.

Acknowledgments

The authors would like to acknowledge the contribution of Dr. Garritt Tucker and Jacob Tavenner from the Computational Materials Science and Design group at the Colorado School of Mines for providing grain boundary structures. We also acknowledge valuable discussions with Dr. Travis Jones from the Fritz Haber Institute of the Max Planck Society. Support of this work under ONR Grant No. N00014-10-1-0838 is gratefully acknowledged.

References

1. W. Kohn. Density functional and density matrix method scaling linearly with the number of atoms. *Physical Review Letters*, 76:3168–3171, Apr 1996.
2. E. Prodan and W. Kohn. Nearsightedness of electronic matter. *Proceedings of the National Academy of Sciences of the United States of America*, 102(33):11635–11638, 2005.
3. E. Prodan. Nearsightedness of electronic matter in one dimension. *Physical Review B*, 73:085108, Feb 2006.
4. Anastassia N. Alexandrova. Divide-and-conquer chemical bonding models for materials: A tool for materials design at the electronic level. *Chemistry of Materials*, 29(20):8555–8565, 2017.
5. Weitao Yang. Direct calculation of electron density in density-functional theory. *Physical Review Letters*, 66:1438–1441, Mar 1991.
6. Yang Wang, G. M. Stocks, W. A. Shelton, D. M. C. Nicholson, Z. Szotek, and W. M. Temmerman. Order-n multiple scattering approach to electronic structure calculations. *Phys. Rev. Lett.*, 75:2867–2870, Oct 1995.
7. A. Thiess, R. Zeller, M. Bolten, P. H. Dederichs, and S. Blügel. Massively parallel density functional calculations for thousands of atoms: Kkrnano. *Phys. Rev. B*, 85:235103, Jun 2012.
8. G te Velde, F M Bickelhaupt, E J Baerends, C Fonseca Guerra, S J A van Gisbergen, J G Snijders, and T Ziegler. Chemistry with ADF. *Journal of Computational Chemistry*, 22(9):931–967, 2001.
9. E J Baerends, T Ziegler, A J Atkins, J Autschbach, D Bashford, A Bérces, F M Bickelhaupt, C Bo, P M Boerrigter, L Cavallo, D P Chong, D V Chulhai, L Deng, R M Dickson, J M Dieterich, D E Ellis, M van Faassen, L Fan, T H Fischer, C Fonseca Guerra, M Franchini, A Ghysels, A Giammona, S J A van Gisbergen, A W Götz, J A Groeneveld, O V Gritsenko, M Grüning, S Gusarov, F E Harris, P van den Hoek, C R Jacob, H Jacobsen, L Jensen, J W Kaminski, G van Kessel, F Kootstra, A Kovalenko, M V Krykunov, E van Lenthe, D A McCormack, A Michalak, M Mitoraj, S M Morton, J Neugebauer, V P Nicu, L Noodleman, V P Osinga, S Patchkovskii, M Pavanello, C A Peeples, P H T Philipsen, D Post, C C Pye, W Ravenek, J I Rodríguez, P Ros, R Rüger, P R T Schipper, H van Schoot, G Schreckenbach, J S Seldenthuis, M Seth, J G Snijders, M Solà, M Swart, D Swerhone, G te Velde, P Vernooijs, L Versluis, L Visscher, O Visser, F Wang, T A Wesolowski, E M van Wezenbeek, G Wiesenekker, S K Wolff, T K Woo, and A L Yakovlev. *ADF2016, SCM, Theoretical Chemistry, Vrije Universiteit, Amsterdam, The Netherlands*. 2016.
10. G. te Velde and E.J. Baerends. Precise density-functional method for periodic structures. *Physical Review B*, 44:7888, 1991.
11. G. Wiesenekker and E.J. Baerends. Quadratic integration over the three-dimensional brillouin zone. *Journal of Physics: Condensed Matter*, 3:6721, 1991.
12. R. F. W. Bader. *Atoms in Molecules: A Quantum Theory*. Clarendon Press: Oxford, UK, 1990.
13. C. F. Matta and R. J. Boyd, editors. *The Quantum Theory of Atoms in Molecules: From Solid State to DNA and Drug Design*. Wiley-VCH Verlag GmbH & Co. KGaA: Weinheim, 2007.
14. Mark E. Eberhart. Are metals made from molecules? *Structural Chemistry*, 28(5):1409–1417, 2017.
15. PAUL G. MEZEY. The holographic electron density theorem and quantum similarity measures. *Molecular Physics*, 96(2):169–178, 1999.
16. J. C. Slater. The Virial and Molecular Structure. *The Journal of Chemical Physics*, 1(10):687–691, 1933.
17. Klaus Ruedenberg and Michael W. Schmidt. Physical Understanding through Variational Reasoning: Electron Sharing and Covalent Bonding. *The Journal of Physical Chemistry A*, 113(10):1954–1968, 2009.
18. R. F. W. Bader and H. J. T. Preston. The kinetic energy of molecular charge distributions and molecular stability. *International Journal of Quantum Chemistry*, 3(3):327–347, 1969.
19. Timothy R. Wilson, Malavikha Rajivmoorthy, Jordan Goss, Sam Riddle, and Mark E. Eberhart. Observing the 3D Chemical Bond and its Energy Distribution in a Projected Space. *ChemPhysChem*, 20(24):3289–3305, 2019.
20. JL Gray. Investigation into the consequences of the failure of a turbine-generator at hinkley point 'a'power station. *Proceedings of the Institution of Mechanical Engineers*, 186(1):379–390, 1972.
21. C Lea and Ernest Demetrios Hondros. Intergranular microchemistry and stress corrosion cracking. *Proceedings of the Royal Society of London. A. Mathematical and Physical Sciences*, 377(1771):477–501, 1981.
22. RP Messmer and CL Briant. The role of chemical bonding in grain boundary embrittlement. *Acta Metallurgica*, 30(2):457–467, 1982.
23. WT Geng, Arthur J Freeman, R Wu, and Gregory B Olson. Effect of mo and pd on the grain-boundary cohesion of fe. *Physical Review B*, 62(10):6208, 2000.
24. Ruqian Wu, Arthur J Freeman, and Gregory B Olson. First principles determination of the effects of phosphorus and boron on iron grain boundary cohesion. *Science*, 265(5170):376–380, 1994.
25. Roger Haydock. The mobility of bonds at metal surfaces (heterogeneous catalysis). *Journal of Physics C: Solid State Physics*, 14(26):3807, 1981.
26. ME Eberhart and DD Vvedensky. Localized grain-boundary electronic states and intergranular fracture. *Physical review letters*, 58(1):61, 1987.
27. Alan Arnold Griffith. Vi. the phenomena of rupture and flow in solids. *Philosophical transactions of the royal society of london. Series A, containing papers of a mathematical or physical character*, 221(582-593):163–198, 1921.
28. AA Griffith, CB Biezeno, and JM Burgers. Proc. 1st int. congr. appl. mech., 1924.
29. A Joffe, MW Kirpitschewa, and MA Lewitzky. Deformation und festigkeit der kristalle. *Zeitschrift für Physik*, 22(1):286–302, 1924.
30. ED Hondeos and D McLean. Cohesion margin of copper. *Philosophical Magazine*, 29(4):771–796, 1974.
31. JD Russell and AT Winter. Orientation effects in embrittlement of copper bicrystals by bismuth. *Scripta metallurgica*, 19(5):575–579, 1985.
32. GH Li and LD Zhang. Relationship between misorientation and bismuth induced embrittlement of [001] tilt boundary in copper bicrystal. *Scripta metallurgica et materialia*, 32(9), 1995.
33. S Chikwembani and J Weertman. Fatigue and fracture of copper-bismuth bicrystals. *Scripta metallurgica*, 19(12):1499–1502, 1985.
34. Hiromi Miura, Hiroshi Nakata, Taku Sakai, Masaharu Kato, and Tsutomu Mori. Temperature dependence of embrittlement of cu [001] symmetrical tilt boundaries induced by bi segregation. *Nippon Kinzoku Gakkaishi (1952)*, 58(5):477–482, 1994.
35. L-S Chang, E Rabkin, BB Straumal, B Baretzky, and W Gust. Thermodynamic aspects of the grain boundary segregation in cu (bi) alloys. *Acta Materialia*, 47(15-16):4041–4046, 1999.
36. L-S Chang, E Rabkin, S Hofmann, and W Gust. Kinetic aspects of the grain boundary segregation in cu (bi) alloys. *Acta materialia*, 47(10):2951–2959, 1999.
37. W Sigle, L-S Ciiang, and W Gusr. On the correlation between grain-boundary segregation, faceting and embrittlement in bi-doped cu. *Philosophical Magazine A*, 82(8):1595–1608, 2002.
38. Gerd Duscher, Matthew F. Chisholm, Uwe Alber, and Manfred Ruhle. Bismuth-induced embrittlement of copper grain boundaries. *Nature Materials*, 3(9):621–626, 09 2004.
39. APC HALLOWES and E VOCE. The mechanism of the embrittlement of deoxidized copper by bismuth. *J Inst Met*, 73:323–376, 1947.
40. Wolfgang Losch. A new model of grain boundary failure in temper embrittled steel. *Acta Metallurgica*, 27(12):1885–1892, 1979.
41. John E. Field. Hot spot ignition mechanisms for explosives. *Accounts of Chemical Research*, 25(11):489–496, 1992.
42. Carlos G. Camara, Juan V. Escobar, Jonathan R. Hird, and Seth J. Putterman. Correlation between nanosecond x-ray flashes and stick–slip friction in peeling tape. *Nature*, 455(7216):1089–1092, 2008.
43. Kenneth S. Suslick and David J. Flannigan. Inside a collapsing bubble: Sonoluminescence and the conditions during cavitation. *Annual Review of Physical Chemistry*, 59(1):659–683, 2008. PMID: 18393682.
44. L. H. Thompson and L. K. Doraiswamy. Sonochemistry: Science and engineering. *Industrial & Engineering Chemistry Research*, 38(4):1215–1249, 04 1999.
45. Arieh Warshel, Pankaz K. Sharma, Mitsunori Kato, Yun Xiang, Hanbin Liu, and Mats H. M. Olsson. Electrostatic basis for enzyme catalysis. *Chemical Reviews*, 106(8):3210–3235, 2006. PMID: 16895325.

A Comments on Computational Approach

Central to this investigation is the comparison of Bader atom energies with energies obtained with band methods. While conceptually undemanding, in practice these comparisons introduces sources of computational error. Band determined energies exploit variational methods while Bader atomic energies are calculated via the virial theorem [1, 2, 3]. In the latter case, even small errors in the calculated core electron energies can produce large total energy errors, which may be minimized using all electron methods and large basis sets. In turn, to facilitate comparison of Bader atom and band energies, to the extent possible, the same all electron basis sets and computational framework should be used for both calculations. The Amsterdam Modeling Suite provides the capabilities necessary to address many of these issues.

The suite utilizes the Amsterdam Density Functional (ADF) package [4, 5] to calculate the electronic structure of clusters, and BAND [6, 7, 5] to model extended crystalline systems. Both codes use the same Slater-type-orbital (STO) basis functions, though some of the basis functions available to ADF are not fully supported by BAND, most consequential, the all electron quadruple zeta basis set including four polarization terms (QZ4P).

This became a factor when modeling the $4d$ transition metals where a QZ4P basis set was required to calculate Bader atom energies accurately. Presumably the large basis set was needed due to the greater number of radial nodes and hence more rapidly varying near nucleus charge density. Nonetheless, since BAND calculations could not be converged using the QZ4P basis set a source of computational error was introduced when comparing BAND determined formation energies with Bader atom energies. As a way of estimating the magnitude of this error, ADF was used to calculate single atom and large cluster total energies for all the $4d$ transition metal elements using both the triple zeta including two polarization terms (TZ2P) and QZ4P basis sets. In general, and not surprisingly, the single atom energies were lower for the larger basis set by about 10 eV. For the larger clusters, the total energy per atom was again lower using the QZ4P basis, but this time by about 10.6 eV per atom. Using the difference between the single atom and large cluster total energies as an approximation to the formation energy, the QZ4P basis set yields a more negative formation energy of approximately 0.6 eV per atom.

As a check on the accuracy of Bader atom energies we used the fact that over a Bader atom the integral of $\nabla^2\rho(r)$ should be identically zero [8, 9]. Deviations greater than 10^{-2} are deemed marginal and indicative of numerical error. We found that the integrated Laplacian of the charge density over the central Bader atom was sensitive to computational parameters. Best results were achieved with a high density Voronoi integration scheme (accint = 6), "very good" density fitting and an appropriate choice of basis set. Even so, in some circumstances the integral of $\nabla^2\rho(r)$ over the central Bader atom was slightly greater than 10^{-2}. However, at all times the same value over the central atom and the atoms of its first coordination shell were within acceptable limits. It is for this reason that we monitored the per atom energy of a "central cluster"—the central atom and its nearest neighbor coordination shell–as a function of changing boundary width. All calculations employed the generalized gradient approximation using the Perdew–Burke–Ernzerhof exchange-correlation functional (GGA PBE) [10]. Finally, the BAND calculations used a quadratic tetrahedron method for numerical integration over the Brillouin zone, sampling a minimum of 16 k points in the irreducible wedge.

B Lattice data

The shell structure for the four lattice types (DC, BCC, HCP, and FCC) discussed in the main text is provided in Tables 1-4 and pictures of representative clusters shown in Figures 1-4.

Table 1: Face-centered cubic (FCC) shell structure. Row 1: Number of the coordination shell. Coordination shell zero is the central atom. Row 2: Number of atoms in coordination shell n. Row 3: Total number of atoms in the cluster of n coordination shells. (Hard sphere representations of some of these clusters are provided in the SI.) Row 4: Radius of the cluster, i.e. distance between the central atom and the atoms of the n^{th} shell in atomic diameters or equivalently nearest neighbor separations.

Coordination shell n	**0**	**1**	**2**	**3**	**4**	**5**	**6**	**7**	**8**	**9**	**10**
Number of n^{th} neighbors	1	12	6	24	12	24	8	48	6	48	24
Total atoms in cluster	1	13	19	43	55	79	87	135	141	189	213
Cluster radius	0	1	$\sqrt{2}$	$\sqrt{3}$	2	$\sqrt{5}$	$\sqrt{6}$	$\sqrt{7}$	$2\sqrt{2}$	3	$\sqrt{10}$

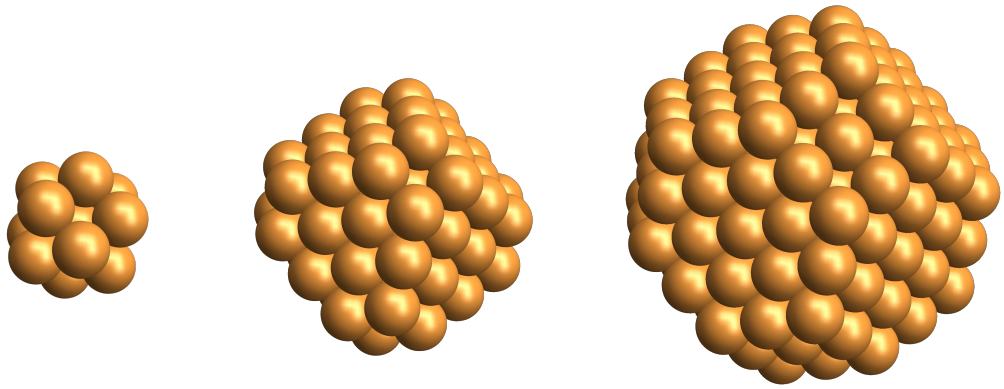

Figure 1: The FCC central 13-atom cluster (left), critical cluster consisting of 5 coordination shells (middle), and the largest cluster consisting of 10 coordination shells (right).

Table 2: Body-centered cubic (BCC) shell structure. Table layout is identical to that of Table 1.

Coordination shell n	**0**	**1**	**2**	**3**	**4**	**5**	**6**	**7**	**8**	**9**	**10**
Number of n^{th} neighbors	1	8	6	12	24	8	6	24	24	24	8
Total atoms in cluster	1	9	15	27	51	59	65	89	113	137	145
Cluster radius	0	1	$2\sqrt{\frac{1}{3}}$	$2\sqrt{\frac{2}{3}}$	$\sqrt{\frac{11}{3}}$	2	$4\sqrt{\frac{1}{3}}$	$\sqrt{\frac{19}{3}}$	$2\sqrt{\frac{5}{3}}$	$2\sqrt{2}$	3

Table 3: Hexagonal close-packed (HCP) shell structure. Table layout is identical to that of Table 1.

Coordination shell n	**0**	**1**	**2**	**3**	**4**	**5**	**6**	**7**	**8**	**9**	**10**	**11**
Number of n^{th} neighbors	1	12	6	2	18	12	6	12	12	6	3	12
Total atoms in cluster	1	13	19	21	39	51	57	69	81	87	90	102
Cluster radius	0	1	$\sqrt{2}$	$2\sqrt{\frac{2}{3}}$	$\sqrt{3}$	$\sqrt{\frac{11}{3}}$	2	$\sqrt{5}$	$\sqrt{\frac{17}{3}}$	$\sqrt{6}$	$\sqrt{\frac{19}{3}}$	$2\sqrt{\frac{5}{3}}$

b

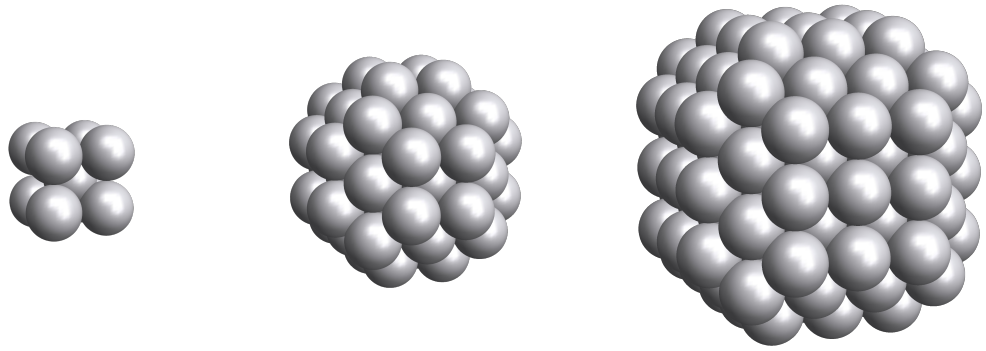

Figure 2: The BCC central 9-atom cluster (left), critical cluster consisting of 5 coordination shells (middle), and the largest cluster consisting of 10 coordination shells (right).

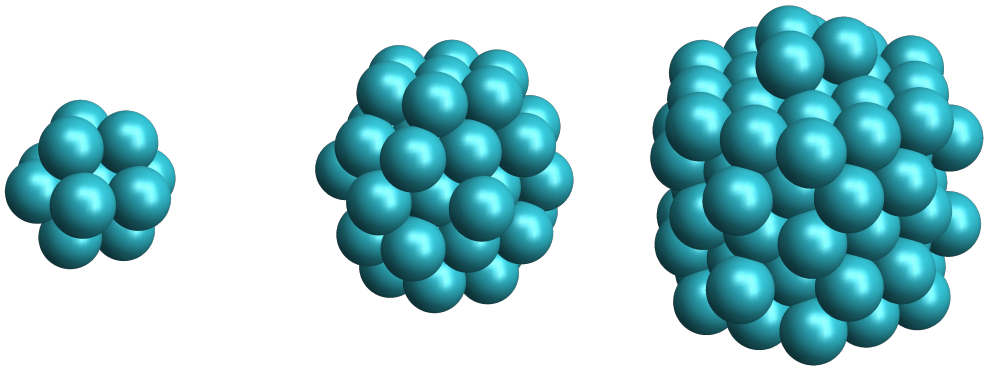

Figure 3: The HCP central 13-atom cluster (left), critical cluster consisting of 5 coordination shells (middle), and the largest cluster consisting of 11 coordination shells (right).

Table 4: Diamond cubic (DC) shell structure. Table layout is identical to that of Table 1.

Coordination shell n	**0**	**1**	**2**	**3**	**4**	**5**	**6**	**7**	**8**	**9**	**10**	**11**
Number of n^{th} neighbors	0	4	12	12	6	12	24	16	12	24	12	8
Total atoms in cluster	1	5	17	29	35	47	71	87	99	123	135	143
Cluster radius	0	1	$2\sqrt{\frac{2}{3}}$	$\sqrt{\frac{11}{3}}$	$4\sqrt{\frac{1}{3}}$	$\sqrt{\frac{19}{3}}$	$2\sqrt{2}$	3	$4\sqrt{\frac{2}{3}}$	$\sqrt{\frac{35}{3}}$	$\sqrt{\frac{43}{3}}$	4

C Element data

Data from which the graphs shown in the main text were constructed are provided in Tables 5-8.

Table 5: Perturbation energies ΔE of the (single) DC cluster investigated, reported in eV.

Element	**Diameter (Å)**	E_f	E_0	ΔE_1	ΔE_2	ΔE_3	ΔE_4	ΔE_5	ΔE_6	ΔE_7	ΔE_8	ΔE_9	ΔE_{11}
Si	2.352	-5.42	-7865.72	-3.05	-9.01	-5.66	-5.55	-6.09	-6.71	-6.67	-6.12	-5.91	-5.79

c

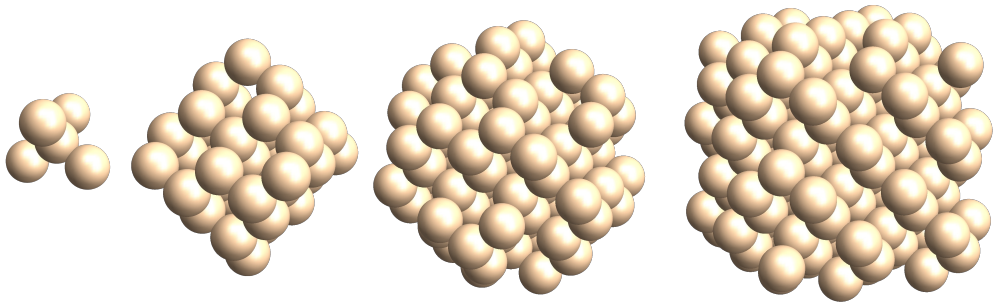

Figure 4: (from the left) The DC central 5-atom cluster, the 4-coordination cluster closing the central atom, the 7-coordination cluster closing the central cluster, and the largest cluster consisting of 11 coordination shells.

Table 6: Perturbation energies ΔE of FCC clusters, reported in eV.

Element	**Diameter (Å)**	E_f	E_0	ΔE_1	ΔE_2	ΔE_3	ΔE_4	ΔE_5	ΔE_6	ΔE_7	ΔE_9
Al	2.864	-3.78	-6587.00	-8.80	-5.86	-7.20	-	-4.65	-	-3.48	-4.08
Cu	2.553	-3.54	-44611.75	-3.64	-5.66	-3.83	-	-4.37	-	-3.56	-3.56
Rh	2.758	-6.78	-127504.31	-3.05	-4.00	-5.87	-	-6.32	-	-7.08	-
Pd	2.751	-3.99	-134362.32	-1.52	-2.22	-4.07	-	-4.71	-	-4.88	-
Ag	2.885	-3.71	-141429.58	-1.38	-2.13	-3.83	-	-3.90	-	-4.01	-

Table 7: Perturbation energies ΔE of BCC clusters, reported in eV.

Element	**Diameter (Å)**	E_f	E_0	ΔE_1	ΔE_2	ΔE_3	ΔE_4	ΔE_5	ΔE_6	ΔE_7	ΔE_8	ΔE_{10}
V	2.624	-8.36	-25665.42	-3.45	-4.35	-7.60	-8.99	-8.74	-8.82	-9.33	-9.04	-8.95
Nb	2.857	-10.22	-102139.80	-2.77	-4.06	-8.71	-9.39	-10.93	-11.02	-11.00	-11.06	-
Mo	2.725	-10.29	-108177.90	-1.57	-9.08	-8.29	-8.82	-10.16	-10.15	-11.51	-11.06	-

Table 8: Perturbation energies ΔE of HCP clusters, reported in eV.

Element	**Diameter (Å)**	E_f	E_0	ΔE_1	ΔE_2	ΔE_3	ΔE_4	ΔE_5	ΔE_6	ΔE_7	ΔE_9	ΔE_{11}
Tc	2.735	-11.52	-114414.78	-3.95	-4.87	-	-9.30	-10.70	-	-11.85	-12.06	-12.52
Ru	2.706	-9.79	-120855.98	-4.66	-5.07	-	-8.67	-9.78	-	-10.84	-11.10	-11.37

d

D Cu-Bi grain boundary data

Grain boundaries are 2-dimensional defects that are present in real materials. They form the interface that separates the orientation in which atoms are stacked; and alter the microstructure, thus affecting performance. The data represented in graphical form in main text is provided in Table 9 and pictures of important clusters in Figure 5/

Table 9: Perturbation energies $\boldsymbol{\Delta E}$ to the 14 atom first coordination shell surrounding the copper or bismuth atom at the center in the $\Sigma 5$ grain boundary clusters Row 1: Number of atoms in the cluster. Row 2: Cluster radii in units of Å. Row 3: per atom energies of central cluster with Bi at center in eV – relative to isolated central cluster. Row 4: per atom energies of central cluster with Cu at center in eV – relative to isolated central cluster.

Number of atoms in cluster	**Cluster radii (Å)**	**ΔE with Bi (eV/atom)**	**ΔE with Cu (eV/atom)**
15	2.906	0.00	0.00
23	4.280	-2.89	0.14
31	4.638	-5.12	-0.39
39	4.683	-6.55	-0.55
47	4.812	-7.61	-0.54
55	5.444	-8.66	-0.54
63	5.725	-9.16	-0.40
71	5.764	-9.32	-0.10
77	5.893	-9.22	0.28
83	6.528	-9.39	0.38
93	6.817	-9.70	0.41
97	6.873	-9.67	0.44

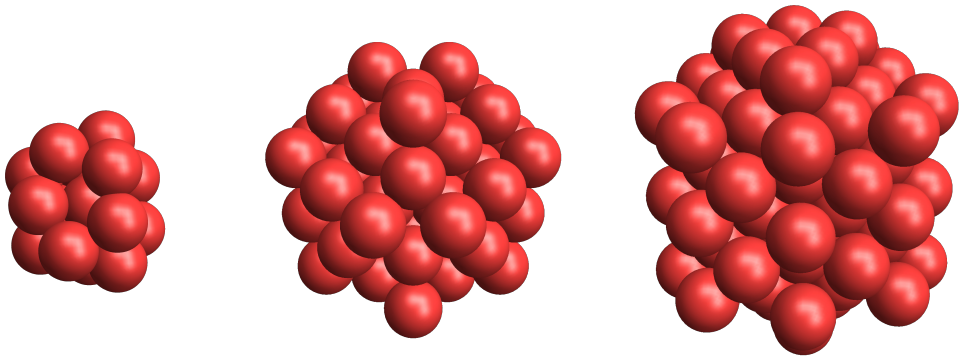

Figure 5: The grain boundary central 15-atom cluster (left), critical cluster consisting of 63 atoms (middle), and the largest cluster consisting of 97 atoms (right).

e

References

[1] J. C. Slater. The Virial and Molecular Structure. *The Journal of Chemical Physics*, 1(10):687–691, 1933.

[2] Klaus Ruedenberg and Michael W. Schmidt. Physical Understanding through Variational Reasoning: Electron Sharing and Covalent Bonding. *The Journal of Physical Chemistry A*, 113(10):1954–1968, 2009.

[3] Juan I. Rodríguez, Paul W. Ayers, Andreas W. Götz, and F. L. Castillo-Alvarado. Virial theorem in the kohn–sham density-functional theory formalism: Accurate calculation of the atomic quantum theory of atoms in molecules energies. *The Journal of Chemical Physics*, 131(2):021101, 2009.

[4] G te Velde, F M Bickelhaupt, E J Baerends, C Fonseca Guerra, S J A van Gisbergen, J G Snijders, and T Ziegler. Chemistry with ADF. *Journal of Computational Chemistry*, 22(9):931–967, 2001.

[5] E J Baerends, T Ziegler, A J Atkins, J Autschbach, D Bashford, A Bérces, F M Bickelhaupt, C Bo, P M Boerrigter, L Cavallo, D P Chong, D V Chulhai, L Deng, R M Dickson, J M Dieterich, D E Ellis, M van Faassen, L Fan, T H Fischer, C Fonseca Guerra, M Franchini, A Ghysels, A Giammona, S J A van Gisbergen, A W Götz, J A Groeneveld, O V Gritsenko, M Grüning, S Gusarov, F E Harris, P van den Hoek, C R Jacob, H Jacobsen, L Jensen, J W Kaminski, G van Kessel, F Kootstra, A Kovalenko, M V Krykunov, E van Lenthe, D A McCormack, A Michalak, M Mitoraj, S M Morton, J Neugebauer, V P Nicu, L Noodleman, V P Osinga, S Patchkovskii, M Pavanello, C A Peeples, P H T Philipsen, D Post, C C Pye, W Ravenek, J I Rodríguez, P Ros, R Rüger, P R T Schipper, H van Schoot, G Schreckenbach, J S Seldenthuis, M Seth, J G Snijders, M Solà, M Swart, D Swerhone, G te Velde, P Vernooijs, L Versluis, L Visscher, O Visser, F Wang, T A Wesolowski, E M van Wezenbeek, G Wiesenekker, S K Wolff, T K Woo, and A L Yakovlev. *ADF2016, SCM, Theoretical Chemistry, Vrije Universiteit, Amsterdam, The Netherlands*. 2016.

[6] G. te Velde and E.J. Baerends. Precise density-functional method for periodic structures. *Physical Review B*, 44:7888, 1991.

[7] G. Wiesenekker and E.J. Baerends. Quadratic integration over the three-dimensional brillouin zone. *Journal of Physics: Condensed Matter*, 3:6721, 1991.

[8] R. F. W. Bader. *Atoms in Molecules: A Quantum Theory*. Clarendon Press: Oxford, UK, 1990.

[9] C. F. Matta and R. J. Boyd, editors. *The Quantum Theory of Atoms in Molecules: From Solid State to DNA and Drug Design*. Wiley-VCH Verlag GmbH & Co. KGaA: Weinheim, 2007.

[10] John P. Perdew, Kieron Burke, and Matthias Ernzerhof. Generalized gradient approximation made simple. *Phys. Rev. Lett.*, 77:3865–3868, Oct 1996.

f